Persistent residential burning-related primary organic particles during wintertime hazes in North China: insights into their aging and optical changes

Lei Liu[1], Jian Zhang[1], Yinxiao Zhang[1], Yuanyuan Wang[1], Liang Xu[1], Qi Yuan[1], Dantong Liu[1], Yele Sun[2], Pingqing Fu[3], Zongbo Shi[4], and Weijun Li[1,*]

[1]Department of Atmospheric Sciences, School of Earth Sciences, Zhejiang University, Hangzhou 310027, China

[2]State Key Laboratory of Atmospheric Boundary Layer Physics and Atmospheric Chemistry, Institute of Atmospheric Physics, Chinese Academy of Sciences, Beijing 100029, China

[3]Institute of Surface-Earth System Science, Tianjin University, Tianjin 300072, China

[4]School of Geography, Earth and Environmental Sciences, University of Birmingham, Birmingham B15 2TT, UK

Correspondence to: Weijun Li (liweijun@zju.edu.cn)

16 **Abstract**

17   Primary organic aerosol (POA) is a major component of $PM_{2.5}$ in winter polluted air in the North

18 China Plain (NCP), but our understanding on the atmospheric aging processes of POA particles and

19 the resulting influences on their optical properties is limited. As part of the Atmospheric Pollution

20 and Human Health in a Chinese Megacity (APHH-Beijing) programme, we collected airborne

21 particles at an urban site (Beijing) and an upwind rural site (Gucheng, Hebei province) in the NCP

22 during 13–27 November 2016 for microscopic analyses. We confirmed that large amounts of light-

23 absorbing spherical POA (i.e., tarball) and irregular POA particles with high viscosity were emitted

24 from the domestic coal and biomass burning at the rural site and were further transported to the urban

25 site during regional wintertime hazes. During the heavily polluted period ($PM_{2.5} > 200$ $\mu g\ m^{-3}$), more

26 than 60% of these burning-related POA particles were thickly coated with secondary inorganic

27 aerosols (named as core–shell POA–SIA particle) through the aging process, suggesting that POA

28 particles can provide surfaces for the heterogeneous reactions of SO_2 and NO_x. As a result, during the

29 heavily polluted period, their average particle-to-core diameter ratios at the rural and urban sites

30 increased to 1.60 and 1.67, respectively. Interestingly, we found that the aging process did not change

31 the morphology and sizes of POA cores, indicating that the burning-related POA particles are quite

32 inert in the atmosphere and can be transported over long distances. Using Mie theory we estimated

33 that the absorption capacity of these POA particles was enhanced by ~1.39 times in the heavily

34 polluted period at the rural and urban sites due to the "lensing effect" of secondary inorganic coatings.

35 We highlight that the "lensing effect" on burning-related POA particles should be considered in

36 radiative forcing models and the governments should continue to promote clean energy in rural areas

37 to effectively reduce primary emissions.

1 Introduction

Atmospheric aerosol particles can affect regional and global energy budgets by scattering or absorbing solar radiation, modify microphysical properties of clouds by acting as cloud condensation nuclei (CCN), and exert adverse effects on human health such as respiratory and cardiovascular diseases (IPCC, 2013; West et al., 2016). With rapid industrialization and urbanization in past decades, severe air pollution characterized by high concentrations of fine particulate matter ($PM_{2.5}$) frequently occurs in China, especially the regional hazes in the North China Plain (NCP), which has received wide concerns from the public, governments, and scientists (Sun et al., 2016). Many previous studies have shown that synergetic effects from extensive emissions of primary particles and gaseous precursors, efficient secondary aerosol formation, regional transport, and unfavorable meteorological conditions are the main factors contributing to haze formation in the NCP (Chang et al., 2018; Liu et al., 2016; Zhong et al., 2019). In particular, long-term measurements have confirmed that wintertime haze episodes in Beijing are commonly initiated by regional transport of air pollutants from the south NCP (e.g., Hebei and Henan provinces) under weak southerly winds and then evolved through the massive secondary aerosol formation via heterogeneous reactions (Ma et al., 2017; Sun et al., 2014; Zheng et al., 2015).

During the regional transport and evolution of haze episodes, complex physical and chemical processes in the atmosphere, such as condensation, coagulation, and heterogeneous reactions, could largely alter the morphology, composition, size, and mixing state of individual particles, which is also known as "particle aging" (Li et al., 2016a). Particle aging could further influence the optical property, health effects, hygroscopicity, and CCN activity of aerosol particles, although different types of particles might have different impacts (Fan et al., 2020; Li et al., 2016b; Riemer et al., 2019). Up to now, most of the studies conducted in the NCP mainly applied various online and offline bulk aerosol analytical techniques (e.g., online aerosol mass spectrometry (AMS) and offline ion chromatography (IC)) to explore mass concentrations, possible sources, and formation mechanisms of different aerosol

63 components, such as sulfate, nitrate, and organics (Chen et al., 2020; Cheng et al., 2016; J. Li et al.,

64 2020; Sun et al., 2016; Wang et al., 2020). However, knowledge on the aging process of aerosol

65 particles remains limited. Therefore, further to document the aging processes of different particles in

66 the NCP through the microscopic individual particle analysis is of great significance for revealing the

67 particle transformation in the atmosphere and better assessing the climatic effects of aerosols (Du et

68 al., 2019; Li et al., 2016a).

69   Field observations have shown that carbonaceous aerosols, including organic aerosol (OA) and

70 black carbon (BC), are the dominant components of $PM_{2.5}$ during heating seasons in the NCP, which

71 usually accounts for more than 50% of the total $PM_{2.5}$ (Liu et al., 2020; P. Liu et al., 2017; Zhang et

72 al., 2020). Source apportionments reveal that residential coal and biomass burning in rural areas are

73 the major contributors to carbonaceous aerosols during wintertime hazes in the NCP (Li et al., 2017).

74 BC is the major light-absorbing aerosol in the atmosphere, which can strongly absorb solar radiation

75 and thus affect the regional and global climate (Bond et al., 2013; D. Liu et al., 2017; Wang et al.,

76 2014). In recent years, a bunch of studies have well documented the aging process of BC particles

77 and revealed that secondary inorganic and organic coatings (e.g., sulfate and organics) can

78 significantly enhance the light absorption capacity of the internally mixed BC particles via the

79 "lensing effect" (Chakrabarty and Heinson, 2018; Wang et al., 2017). Recently, light-absorbing

80 organic aerosols, also known as brown carbon (BrC), have been reported to be ubiquitous in the

81 atmosphere in the NCP (Wang et al., 2018; Xie et al., 2019). Many studies have demonstrated that

82 primary OA (POA) emitted from residential coal and biomass burning is the major source of BrC,

83 and the chemical composition and optical properties of BrC in freshly emitted POA as well as the

84 BrC in the ambient atmosphere were analyzed in detail using bulk techniques such as mass

85 spectrometry and UV−visible spectrophotometry (M. Li et al., 2019; X. Li et al., 2020; Song et al.,

86 2018; Sun et al., 2017; Yan et al., 2017). However, only a few studies characterized microscopic

87 properties such as the morphology and mixing state of fresh burning-related POA particles by

88　transmission electron microscopy (TEM) (L. Liu et al., 2017; Zhang et al., 2018). The abundance and

89　aging process of burning-related POA particles in the atmosphere and the resulting influences on their

90　optical properties remain unknown in the NCP.

91　　This study, as part of the Atmospheric Pollution and Human Health in a Chinese Megacity

92　(APHH-Beijing) programme (Shi et al., 2019), aims to explore the atmospheric aging process of POA

93　particles emitted from the residential coal and biomass burning in rural areas following the regional

94　transport and evolution of haze episodes. Individual particle samples were collected in urban Beijing

95　and the surrounding rural regions during the winter campaign and then were analyzed by microscopic

96　methods to obtain the morphology, composition, size, and mixing state of different individual particle

97　types. Besides, bulk analyses of aerosol chemical composition were also conducted to help understand

98　the evolution of haze episodes. We found that large amounts of POA particles were emitted from the

99　domestic coal and biomass burning in winter in the NCP. For the first time, we characterized the aging

100　process of such burning-related POA particles based on microscopic analyses and Mie theory was

101　used to further explore the resulting influences on their optical properties.

102　**2 Experimental methods**

103　**2.1 Sampling sites and sample collections**

104　　Field observations were carried out simultaneously at the Beijing (BJ) urban site (39°58'27" N,

105　116°22'16" E) and Gucheng (GC) rural site (39°08'58" N, 115°44'00" E) during 13–27 November

106　2016. Locations of two sampling sites in the NCP are displayed in Fig. 1a. The BJ urban site, located

107　on the rooftop of a two-story building (8 m above ground level (a.g.l.)) in the Tower Division of the

108　Institute of Atmospheric Physics, Chinese Academy of Sciences, is between the north 3rd and 4th

109　ring roads and surrounded by commercial area and residential apartments (Fig. 1b). The GC rural site,

110　located on the rooftop of a three-story building (12 m a.g.l.) at the Gucheng Integrated Ecological–

111　Meteorological Observation and Experimental Station of the Chinese Academy of Meteorological

112　Sciences in Dingxing county, Hebei province, is 120 km to the southwest of the BJ urban site and

113   surrounded by many villages and farmlands (Fig. 1c). Detailed information about the two sampling

114   sites can be found in the introduction paper of APHH-Beijing programme (Shi et al., 2019). The 24-

115   h backward trajectories of air masses ending at the height of 100 m (a.g.l.) over the BJ urban site (Fig.

116   1a) were calculated using the NOAA Air Resources Laboratory's HYbrid Single-Particle Lagrangian

117   Integrated Trajectory (HYSPLIT) model (Stein et al., 2016).

118   At the BJ urban site, the species in non-refractory submicron aerosols (NR-PM$_1$) including

119   organic matter (OM), SO_4^{2-}, NO_3^-, NH_4^+, and Cl^- were measured by a high-resolution aerosol mass

120   spectrometer (HR-AMS, Aerodyne Inc., USA). At the GC rural site, PM$_{2.5}$ samples were collected

121   twice a day during the daytime (8:00 to 20:00) and nighttime (20:00 to 8:00 the next day) onto 90

122   mm-diameter quartz filters (Pallflex 7204, Pall Corporation, USA) using a medium-volume sampler

123   (TH-150A, Wuhan Tianhong Instruments Co., Ltd., China) at a flow rate of 100 L min^{-1}. Field blank

124   samples were collected for approximately 15 min without starting the sampler. The filters were

125   prebaked at 450°C for 6 h before sampling to remove any possible contaminants. All the collected

126   samples were sealed individually in aluminum foil bags and stored in a refrigerator at −20 °C for

127   further analyses.

128   Individual particle samples were collected onto copper (Cu) TEM grids coated by formvar and

129   carbon films (carbon type-B, 300 mesh, Beijing XXBR Technology Co., Ltd., China) at the GC rural

130   and BJ urban sites using an individual particle sampler (DKL-2, Qingdao Genstar Electronic

131   Technology Co., Ltd., China) at a flow rate of 1 L min^{-1}. The DKL-2 sampler consists of a single-

132   stage impactor with a 0.5 mm-diameter jet nozzle. Sampling duration ranged from 8 s to 3 min

133   depending on the pollution levels to avoid overlap of particles on the TEM grids. Individual particle

134   samples were placed in a clean and airtight container with controlled temperature (T, 25±1°C) and

135   relative humidity (RH, 20±3%) for further analyses. The detailed information about the individual

136   particle samples collected at the two sites is listed in Table S1.

137   Meteorological parameters including T, pressure (P), RH, wind speed (WS), and wind direction

(WD) were recorded every 5 min at two sampling sites using a pocket weather station (Kestrel 5500, Nielsen-Kellermann Inc., USA). Hourly concentrations of $PM_{2.5}$ and gaseous pollutants (i.e., SO_2, NO_2, CO, and O_3) during the sampling period at two monitoring stations (i.e., Dingxing government station: 39°15'42" N, 115°48'06" E; Beijing Olympic center station: 40°00'11" N, 116°24'25" E) close to GC rural and BJ urban sites were downloaded from the website of air quality online monitoring and analysis platform (https://www.aqistudy.cn/). All the data in this study are presented at the Beijing local time (UTC+8).

2.2 $PM_{2.5}$ chemical analysis

$PM_{2.5}$ samples collected at the GC rural site were analyzed to obtain their water-soluble inorganic ions (WSIIs), organic carbon (OC), and elemental carbon (EC). For the analysis of WSIIs, two 16 mm-diameter punches from each $PM_{2.5}$ sample were put into a vial, followed by adding 20 mL deionized water (18.2 MΩ). Then these vials were placed in an ultrasonic water bath for 30 min to extract WSIIs. The solutions were further filtered using PTFE syringe filters with 0.45 μm pore size to remove insoluble components and then analyzed by an ion chromatography system (Dionex ICS 600, ThermoFisher Scientific, USA). Finally, concentrations of three anions (Cl^-, SO_4^{2-}, and NO_3^-) and five cations (Na^+, NH_4^+, K^+, Mg^{2+}, and Ca^{2+}) were obtained. Concentrations of OC and EC in $PM_{2.5}$ samples were determined by analyzing a 1×1.5 cm^2 punch from each filter with an OCEC analyzer (Model 5L, Sunset Laboratory Inc. USA), which adopted the NIOSH870 temperature protocol with thermal–optical transmittance for charring correction. The OM concentration was estimated via multiplying OC concentration by a factor of 1.6, based on the previous studies (Xing et al., 2013; Zheng et al., 2015).

2.3 AMS data analysis

The HR-AMS V-mode data were analyzed using standard data analysis software (PIKA V1.56D). A constant collection efficiency (CE) of 0.5, similar to the previous study conducted in winter at the BJ site (Sun et al., 2014), was applied to the HR-AMS datasets to obtain mass concentrations of NR-

163   PM_1 species. The relative ionization efficiencies used for OM, SO_4^{2-}, NO_3^-, NH_4^+, and Cl^- were 1.4,

164   1.2, 1.1, 5.0, and 1.3, respectively. Positive matrix factorization (PMF) is a receptor model to identify

165   potential sources without local source profiles provided (Xu et al., 2020). PMF was performed on the

166   high-resolution mass spectra of organics measured by HR-AMS. Six OA factors were identified

167   including fossil fuel-related OA (FFOA), cooking OA (COA), biomass burning OA (BBOA),

168   oxidized primary OA (OPOA), oxygenated OA (OOA), and aqueous-phase OOA (aqOOA). Detailed

169   information on the processing of HR-AMS data can be found in the related paper during the same

170   campaign (Xu et al., 2019).

171   **2.4 Individual particle analysis**

172   Individual particle samples were analyzed using TEM (JEM-2100, JEOL Ltd., Japan) operated

173   at a 200 kV accelerating voltage to acquire morphology and sizes of individual particles and mixing

174   state (i.e., internally or externally mixed) of different aerosol components within one individual

175   particle. TEM is equipped with an energy-dispersive X-ray spectrometer (EDS, INCA X-Max^N 80T,

176   Oxford Instruments, UK) to semi-quantitatively detect the elemental composition of individual

177   particles with atomic number greater than six ($Z \geq 6$). It should be noted that Cu peaks in the EDS

178   spectra are not considered due to the interference from the Cu substrate of TEM grids. The distribution

179   of aerosol particles on TEM grids is not uniform, with particle size decreasing from the center to the

180   edge of the distribution area. Therefore, to ensure the analyzed particles are representative, five grid

181   meshes from the center to the edge of the particle distribution area in each sample were selected to

182   conduct TEM analysis. TEM images were manually processed by the RADIUS 2.0 software (EMSIS

183   GmbH, Germany) to determine the particle types, areas, perimeters, and equivalent circle diameters

184   (ECD). After a labor-intensive operation, a total of 1197 particles at the BJ urban site and 2443

185   particles at the GC rural site were analyzed.

186   Scanning electron microscope (SEM, Ultra 55, Carl Zeiss Microscopy GmbH, Germany) was

187   operated at the 10 kV accelerating voltage and secondary electron (SE2) mode to observe the particle

188 surface topography. Furthermore, particles were imaged at a tilt angle of 75° to realize the

189 visualization of their morphology in the vertical dimension.

190 **2.5 Optical property calculation**

191   Mie theory has been widely used to calculate the optical properties of individual particles by

192 assuming a spherical core–shell structure (Chylek et al., 2019; Wu et al., 2018; Yu et al., 2019). In

193 this study, the light absorption cross sections (ACS) of internally mixed POA particles with secondary

194 inorganic aerosol (SIA) shell (named as core–shell POA–SIA particle), as well as the POA cores and

195 bare POA particles at the wavelength of 550 nm were calculated with BHCOAT Mie code (Bohren

196 and Huffman, 1983). Details for the classification of POA and POA–SIA particles, please refer to

197 Section 3.2. For the core–shell POA–SIA particles, a refractive index (RI) of $1.55-0i$ for non-light-

198 absorbing SIA coating (Denjean et al., 2014) and $1.67-0.27i$ for light-absorbing POA core (Alexander

199 et al., 2008) were adopted at the wavelength of 550 nm; and the ECD of each POA–SIA particle and

200 its POA core obtained from the TEM images were used respectively as the input particle diameter

201 (D_p) and core diameter (D_c) in the Mie calculation, which made the calculation sufficient to

202 approximate reality. Because a core–shell structure is considered in the Mie model (Bond et al., 2006),

203 for the uncoated POA particles (including POA cores without SIA shell and bare POA particles), the

204 ECD of each POA particle and one-tenth of it were input as the D_p and D_c, respectively. Then in the

205 case of vanishing the refractive index difference between the shell and core (i.e., POA core and POA

206 shell, RI=$1.67-0.27i$), the Mie model can be applied to homogeneous particles. Besides, we also

207 constructed models of core–shell POA–SIA particles with different POA core diameters (i.e., D_c=100,

208 200, 300, 400, 500, 700, 900, 1100, 1300, and 1500 nm) and particle-to-core diameter ratios (i.e.,

209 D_p/D_c ranged from 1 to 6 with an interval of 0.1), and calculated their ACS to further explore the

210 effects of D_c and D_p/D_c changes on the light absorption enhancement factors (E_{abs}) of POA particles.

211   After running the Mie calculation, attenuation efficiency (Q_{atn}), scattering efficiency (Q_{sca}), and

212 absorption efficiency (Q_{abs}) of an individual particle were output with their definitions as follows

(Aden and Kerker, 1951; Toon and Ackerman, 1981):

$$Q_{atn} = \left(\frac{2}{x^2}\right) \sum_{n=1}^{\infty} (2n+1)[\text{Re}(a_n+b_n)] \tag{1}$$

$$Q_{sca} = \left(\frac{2}{x^2}\right) \sum_{n=1}^{\infty} (2n+1)(|a_n|^2+|b_n|^2) \tag{2}$$

$$Q_{abs} = Q_{atn} - Q_{sca} \tag{3}$$

where $x = \frac{\pi D}{\lambda}$, is the dimensionless size parameter of the particle diameter D and the wavelength of incident light λ; a_n and b_n are calculated from Riccati–Bessel functions of the particle sizes and refractive indices (Bohren and Huffman, 1983); The symbol Re denotes the real part of the complex quantity a_n+b_n. The ACS of a particle can be obtained via multiplying the Q_{abs} by geometric cross section of the particle shown as follow:

$$\text{ACS} = Q_{abs} \times \frac{\pi D^2}{4} \tag{4}$$

3 Results and Discussion

3.1 Overview of a regional haze episode

A typical regional heavy haze episode in the NCP was observed at the GC rural and BJ urban sites during 22–27 November 2016. Based on variations of hourly PM$_{2.5}$ concentrations, three pollution levels are defined: clean (PM$_{2.5} \leq 75$ µg m^{-3}), moderate pollution (75 µg m^{-3} < PM$_{2.5} \leq 200$ µg m^{-3}), and heavy pollution (PM$_{2.5} > 200$ µg m^{-3}). According to the above criteria, we classified clean period (21 Nov. 0:00 to 22 Nov. 19:00) and heavily polluted period (22 Nov. 20:00 to 27 Nov. 10:00) at the GC rural site; clean period (21 Nov. 0:00 to 24 Nov. 9:00), moderately polluted period (24 Nov. 10:00 to 25 Nov. 16:00), and heavily polluted period (25 Nov. 17:00 to 27 Nov. 2:00) at the BJ urban site (Fig. 2). Furthermore, we divided the heavily polluted period at the GC rural site into the early stage (22 Nov. 20:00 to 23 Nov. 20:00), middle stage (23 Nov. 20:00 to 24 Nov. 20:00), and late stage (24 Nov. 20:00 to 27 Nov. 8:00) based on the evolution of chemical species in PM$_{2.5}$ (Fig.

235 2a). The average meteorological parameters and mass concentrations of $PM_{2.5}$, aerosol chemical

236 species, OA factors, and gaseous pollutants in different periods at two sampling sites are summarized

237 in Table S2.

238 Strong northwesterly winds ($> 4 \text{ m s}^{-1}$) accompanied with rain and snow invaded the NCP during

239 20−21 November (Fig. S1), leading to fast dispersion of air pollutants (Figs. 2 and S2). The low T

240 (-8 to 5°C) and WS ($< 2 \text{ m s}^{-1}$) were displayed after the cold front (Fig. S1), which can facilitate the

241 accumulation of air pollutants (Zhong et al., 2019). At the GC rural site, $PM_{2.5}$ concentration began

242 to increase at 18:00 on 22 November and quickly reached a peak of 394 $\mu\text{g m}^{-3}$ within six hours (Fig.

243 2a). $PM_{2.5}$ chemical analysis reveals that OM (252.8 $\mu\text{g m}^{-3}$) accounted for 83% of the $PM_{2.5}$ in the

244 nighttime sample on 22 November (i.e., 22 Nov. 20:00 to 23 Nov. 8:00), causing the fast transition

245 from the clean to heavily polluted period directly (Figs. 2a and S3a). In the early stage of heavily

246 polluted period, the average $PM_{2.5}$ concentration (288.3 $\mu\text{g m}^{-3}$) increased by a factor of seven

247 compared with that (39.8 $\mu\text{g m}^{-3}$) in the clean period, with OM being the largest contributor (185.1

248 $\mu\text{g m}^{-3}$) followed by SIA (i.e., sum of SO_4^{2-}, NO_3^-, and NH_4^+; 36.4 $\mu\text{g m}^{-3}$) (Table S2). At the BJ

249 urban site, the air quality remained clean before 24 November under continuous northerly winds (Figs.

250 2b and S1b). With prevailing winds changing from northerly to southerly on 24 November (Fig. S1),

251 polluted air parcels in the south of NCP were transported to Beijing (Fig. 1a), which has also been

252 confirmed by another study conducted in the APHH-Beijing winter campaign (Du et al., 2019). Thus,

253 the concentrations of $PM_{2.5}$, chemical species in NR-PM_1, CO, and SO_2 at the BJ urban site increased

254 simultaneously and sharply from 09:00 on 24 November, causing the transition from the clean period

255 to the moderately polluted period (Figs. 2b and S2b). The average $PM_{2.5}$ concentration in the

256 moderately polluted period was 111.0 $\mu\text{g m}^{-3}$, 10 times higher than that (10.8 $\mu\text{g m}^{-3}$) in the clean

257 period, and the OM and SIA contributed equally in NR-PM_1 with their average concentrations being

258 44.4 and 43.4 $\mu\text{g m}^{-3}$, respectively (Table S2). Following the haze evolution, $PM_{2.5}$ levels increased

259 gradually to 312.3 and 396.8 $\mu\text{g m}^{-3}$ in the middle and late stages of heavily polluted period at the

260   GC rural site and to 281.0 μg m^{-3} in the heavily polluted period at the BJ urban site (Fig. 2 and Table

261   S2). Contrasting to the above transition periods at two sampling sites, we found that the SIA

262   concentration increased significantly, meanwhile, the OM concentration only slightly increased at the

263   GC rural and BJ urban sites with the consistent decreasing WS and increasing RH during the heavily

264   polluted period (Figs. 2 and S1). In a word, we observed that the SIA fraction in fine particles

265   increased and the OM fraction decreased following the haze evolution (Fig. S3).

266   The concentrations and fractions of OM and EC at nighttime were much higher than those at

267   daytime during the whole haze episode at the GC rural site (Figs. 2a and S3a), suggesting the

268   continuous strong local combustion emissions at nighttime. Furthermore, the concentration of Cl$^-$ (8–

269   22 μg m^{-3}) was much higher than that of K$^+$ (1–3 μg m^{-3}) (Fig. 2a), which suggests more contributions

270   from coal combustion than biomass burning at the GC rural site (Sun et al., 2014; Zhang et al., 2020).

271   Based on the field investigation and PM$_{2.5}$ analysis, we concluded that the explosive increase of PM$_{2.5}$

272   at the GC rural site was initiated by strong local emissions and accumulation of POA from residential

273   coal combustion for heating and a small fraction of biomass burning for cooking in rural areas. The

274   PMF analysis shows that FFOA and BBOA (14.6–30.6 μg m^{-3}) contributed significantly (> 30%) to

275   OM in the polluted period at the BJ urban site (Fig. S4 and Table S2), suggesting that POA emitted

276   in rural areas were transported to Beijing under southerly winds. In summary, bulk analyses show

277   that POA from residential coal and biomass burning consistently contributed to the regional haze, and

278   SIA produced from the secondary formation had an increasing contribution at higher RH following

279   the haze evolution.

280   **3.2 Classification of individual particle types**

281   In this study, TEM observations show abundant spherical and irregular particles comprised of C,

282   O, and Si elements during this haze episode (Fig. 3a). These particles are stable under strong electron

283   beams and appear as dark features in TEM images, reflecting their high thickness and refractory

284   properties (Ebert et al., 2016; Liu et al., 2018). The SEM image acquired at a 75° tilt angle shows that

these particles did not deform upon impaction and retained high vertical dimensions (Fig. 4), indicating that these particles are in a solid state with high viscosity (Reid et al., 2018; Wang et al., 2016). By contrast, the secondary particles (i.e., SIA and organic coating) became flat on the substrate (Fig. 4). Previous studies have confirmed that these solid spherical and irregular particles are POA particles emitted from coal and biomass burning (L. Liu et al., 2017; Zhang et al., 2018), especially the spherical POA particles as shown in Fig. 3a-1 are defined as tarballs containing light-absorbing BrC (Adachi et al., 2019; C. Li et al., 2019; Pósfai et al., 2003; Zhang et al., 2018). Tarballs (Fig. 3a-1) and irregular POA particles (Fig. 3a-2) are both burning-related POA particles and have similar chemical composition and physical characteristics under the TEM despite their different shapes, thus in this study, we consider that irregular POA particles also contain light-absorbing BrC like tarballs.

Other typical individual particle types, such as SIA (Fig. 3b), mineral (Fig. 3c), soot (Fig. 3d), and fly ash/metal (Fig. 3e) particles were also classified during this haze episode. The detailed classification criteria of these particle types derived from the TEM images and their sources can be found in our previous paper (Li et al., 2016a). It should be noted that some SIA particles were coated with secondary organic coatings (Fig. 3b) which were produced from the chemical oxidation of volatile organic compounds (Li et al., 2016b). TEM observations further show the internal mixture of POA or soot particles with SIA, i.e., POA–SIA (Fig. 3f) and soot–SIA (Fig. 3g). To better understand the number variations of different particle types, we classified bare POA and POA–SIA particles as the POA-containing particles, and bare soot and soot–SIA particles as soot-containing particles.

3.3 Relative abundance of individual particle types

Figure 5 shows number fractions of different particle types in different periods at GC rural and BJ urban sites. At the GC rural site, POA-containing and soot-containing particles were the major particle types with their corresponding contributions being 37.6% and 35.9% by number, followed by SIA particles (22.4%) in the clean period. When the haze episode occurred at the GC rural site, POA-containing particles became dominant in the early stage of heavily polluted period and its

number fraction (64.8%) was nearly twice that (37.6%) in the clean period (Fig. 5a). This result agrees

well with the bulk $PM_{2.5}$ analysis which shows a sharp increase in OM concentration in the early

stage of heavily polluted period (Fig. 2a). With increasing pollution levels from the early stage to the

late stage of heavily polluted period, the fraction of POA-containing particles slightly decreased from

64.8% to 50.8%, by contrast, the fraction of SIA particles increased from 4.6% to 12.4% (Fig. 5a).

The variations of POA-containing and SIA particles are similar to the results from the bulk $PM_{2.5}$

analysis as shown in Fig. 2a.

At the BJ urban site, the contribution of POA-containing particles (15.1%) in the clean period

was much lower than that (37.6%) at the GC rural site (Fig. 5). Following the transition from the

clean period to the moderately polluted period at the BJ urban site, the fraction of POA-containing

particles (66.2%) increased significantly by more than a factor of four compared with that (15.1%) in

the clean period. Meanwhile, fractions of soot-containing, mineral, and SIA particles decreased

largely. When the pollution level changed to the heavily polluted period, similar to the situation at the

GC rural site, the fraction of SIA particles increased from 7.8% to 13.2% and the fraction of POA-

containing particles decreased slightly from 66.2% to 52.8% (Fig. 5b). Overall, the individual particle

analysis results agree well with changes in aerosol chemical components obtained by the bulk analysis

as shown in Fig. 2. Furthermore, individual particle analysis reveals that POA-containing particles

dominated (> 50% by number) in the rural and urban air during the regional wintertime haze episode.

3.4 Atmospheric aging of POA particles

TEM images clearly show the morphology and mixing state of individual particles in different

polluted periods at GC rural and BJ urban sites (Fig. 6). At the GC rural site, we found that large

amounts of bare POA particles, especially tarballs occurred in the early stage of heavily polluted

period (Fig. 6a). Based on the integrated analyses of individual particles and bulk samples, we

confirmed that POA particles emitted from the intense domestic coal and biomass burning for heating

and cooking contributed significantly to the deterioration of air quality in rural areas. When the haze

335   episode evolved into the late stage of heavily polluted period, we found that most of the POA particles

336   were coated with SIA (i.e., POA–SIA particle) forming the core–shell structure (Fig. 6b). This result

337   indicates that POA particles in the regional haze layer provided surfaces for the heterogeneous

338   reactions of SO_2 and NO_x, which promotes the formation of SIA on POA particles in the humid

339   polluted air (Ebert et al., 2016; Zhang et al., 2017).

340   Following the regional transport of polluted air masses from the south to the north of the NCP,

341   abundant POA particles occurred in the moderately polluted period at the BJ urban site (Fig. 6c).

342   Therefore, we conclude that the POA particles emitted in the rural areas in the south of the NCP could

343   be transported to the BJ urban site and significantly affect the urban air quality. Following the haze

344   evolution, similar to those at the GC rural site, the POA particles aged and became core–shell POA–

345   SIA particles at the BJ urban site in the heavily polluted period (Fig. 6d).

346   Based on the mixing state of POA-containing particles, we found that following evolution of the

347   haze episode, the fraction of bare POA particles was reduced by twice from 91.4% in the early stage

348   to 39.6% in the late stage of heavily polluted period at the GC rural site, and the fraction of POA–

349   SIA particles correspondingly increased by seven times from 8.6% to 60.4% (pie charts in Fig. 7).

350   Similarly, at the BJ urban site, the fraction of bare POA particles decreased from 70.4% in the

351   moderately polluted period to 31.4% in the heavily polluted period, and the fraction of POA–SIA

352   particles increased correspondingly from 29.6% to 68.6% (pie charts in Fig. 7). Consequently, the

353   average size of POA-containing particles increased from 505 nm in the early stage to 837 nm in the

354   late stage of heavily polluted period at the GC rural site and from 443 nm in the moderately polluted

355   period to 732 nm in the heavily polluted period at the BJ urban site (Fig. 7a). Interestingly, the average

356   sizes of uncoated POA particles (i.e., POA cores and bare POA) remained similar following the haze

357   evolution, with their respective values being 469, 508, and 465 nm in the early, middle, and late stages

358   of heavily polluted period at the GC rural site and 381 and 379 nm in the moderately and heavily

359   polluted periods at the BJ urban site (Fig. 7b). The average sizes of uncoated POA particles at the BJ

360 urban site were slightly smaller than those at the GC rural site, which is reasonable because the fresh

361 POA particles with larger sizes could be collected at the GC rural site close to emission sources and

362 larger ones are more likely to be removed during the regional transport (Seinfeld and Pandis, 2006).

363 Adachi et al. (2018) reported that tarballs retained their spherical shapes and the particle masses and

364 sizes did not change largely when heated to 300°C in TEM. As a result, we conclude that the POA

365 particles should be quite physically stable and chemically inert in the atmosphere, which can be

366 transported over long distances.

367   The D_p/D_c ratio can be used to indicate the aging degree of POA-containing particles in the

368 atmosphere (Chen et al., 2017; Li et al., 2011). By calculating the D_p/D_c ratio, we realized

369 quantification of the aging degree of POA-containing particles as shown in Fig. 8. In the early stage

370 of heavily polluted period at the GC rural site, the POA-containing particles were mainly fresh bare

371 POA particles with a fraction of 91.4% (Fig. 7), therefore, the average D_p/D_c ratio was close to one

372 (1.02). Following the haze evolution at the GC rural and BJ urban sites, average D_p/D_c ratios increased

373 from 1.08 in the middle stage to 1.60 in the late stage of heavily polluted period at the GC rural site,

374 and from 1.11 in the moderately polluted period to 1.67 in the heavily polluted period at the BJ urban

375 site. The results indicate that POA particles were thickly coated with SIA due to the particle aging

376 process. Here we can obtain two conclusions based on the individual particle analysis: (1) more POA

377 particles continuously aged and were coated with SIA following the haze evolution; (2) the SIA

378 coating gradually grew through the heterogeneous conversion of gaseous precursors (e.g., SO_2 and

379 NO_x) in the polluted air. Therefore, the aging process of individual POA particles in wintertime hazes

380 well reflects the regional haze evolution in the NCP.

381 **3.5 Changes in light absorption of POA particles**

382   It is well known that organic aerosols emitted from coal and biomass burning are the main source

383 of light-absorbing BrC (M. Li et al., 2019; Lin et al., 2016; Sun et al., 2017). Recently, some

384 observation and modelling works show that BrC in haze layers over the NCP can affect the regional

385   energy budget (Feng et al., 2013; Wang et al., 2018; Xie et al., 2019). However, there is no answer on

386   how the aging process of burning-related light-absorbing POA particles influences their optical

387   absorption in the regional haze. Here using Mie theory we further explored variations in the optical

388   absorption of individual POA particles following the haze evolution at the GC rural and BJ urban

389   sites (Fig. 9). It should be noted that another RI of $1.84-0.21i$ for tarballs was reported by Hoffer et

390   al. (2016). The average Mie calculation results at the GC rural and BJ urban sites obtained by the RIs

391   of $1.67-0.27i$ (used in this study) and $1.84-0.21i$ were compared and we found that the two RIs only

392   cause little differences between the results (Table S3). Therefore, only the results from the RI of

393    $1.67-0.27i$ were used and discussed in this study.

394   At the GC rural site, the average ACS of individual POA-containing particles under the actual

395   scenario (ACS_{actual}) in the early, middle, and late stages of heavily polluted period were estimated to

396   be 3.09×10^{-14}, 3.97×10^{-14}, and 4.43×10^{-14} m^2, respectively (Fig. 9a). If all the POA-containing

397   particles were not coated with SIA in each period (i.e., particle non-aging scenario), the corresponding

398   average ACS of individual uncoated POA particles ($ACS_{non-aging}$) were 3.01×10^{-14}, 3.53×10^{-14}, and

399   3.18×10^{-14} m^2, respectively (Fig. 9a). Therefore, we obtained that the E_{abs} (i.e., ratio of ACS_{actual} to

400    $ACS_{non-aging}$) were 1.02, 1.12, and 1.39 in the early, middle, and late stages of heavily polluted period,

401   respectively, at the GC rural site (Fig. 9a). Similarly, at the BJ urban site, the E_{abs} were 1.10 and 1.39

402   in the moderately and heavily polluted periods, respectively, with the corresponding average ACS_{actual}

403   being 2.06×10^{-14} and 3.00×10^{-14} m^2 and $ACS_{non-aging}$ being 1.86×10^{-14} and 2.15×10^{-14} m^2 (Fig. 9b).

404   The light absorption capacity of individual POA particles at the BJ urban site was a little lower than

405   that at the GC rural site (Fig. 9), which was mainly attributed to the smaller sizes of POA particles at

406   the BJ urban site (Fig. 7).

407   To better understand the influence of SIA-coating thickness and POA-core diameter on the light

408   absorption of POA–SIA particles, we modelled the variations in E_{abs} of POA–SIA particles (i.e., ratio

409   of $ACS_{POA–SIA}$ to $ACS_{POA\ core}$) with different D_c as a function of D_p/D_c ratios (Fig. 10). Results show

410 that E_{abs} is sensitive to the changes in both D_c and D_p/D_c ratio. When $D_p/D_c < 1.5$, the E_{abs} increases

411 sharply with the increase of D_p/D_c ratio for different POA core sizes; but when $D_p/D_c > 1.5$, the E_{abs}

412 does not show an increase any more for particles with $D_c > 200$ nm, and the E_{abs} is limited to between

413 1.5 and 2 for particles with D_c ranging from 200 to 1500 nm (Fig. 10). The diameters of observed

414 POA cores at GC rural and BJ urban sites in this study were mainly in the range of 200 to 800 nm

415 (Fig. 7), thus the E_{abs} of observed POA–SIA particles in the NCP were mostly below 1.75 (Fig. 10).

416 All the above results indicate that the atmospheric aging process could significantly improve the light

417 absorption capacity of POA particles along with the evolution of haze episodes due to the "lensing

418 effect" of SIA coating.

419 **4 Conclusions and implications**

420   This study demonstrates that primary pollutants especially large amounts of POA particles

421 emitted from the residential coal and biomass burning in rural areas initiated the wintertime regional

422 haze episode in the NCP. The presence of abundant burning-related POA particles in the atmosphere

423 could further provide surfaces for heterogeneous reactions promoting the large production of SIA

424 under stagnant metrological conditions with high RH, which further elevated the pollution level.

425 Compared with the tarballs which have been confirmed as BrC with strong light-absorbing capacities

426 in previous studies (Adachi et al., 2019; C. Li et al., 2019), the spherical POA (i.e., tarball) and

427 irregular POA particles observed in this study can better represent burning-related light-absorbing

428 primary organic particles in the wintertime hazes. Therefore, the ubiquitous light-absorbing POA

429 particles in the atmosphere of NCP unquestionably affect the energy balance (Feng et al., 2013). We

430 found that burning-related POA particles remained quite stable during the regional transport from the

431 rural areas to urban Beijing in the NCP and were coated with SIA through the atmospheric aging

432 process in the haze layer, which could significantly enhance the light absorption capacity of POA

433 particles via the "lensing effect" of SIA coating. We estimated that E_{abs} values were within the upper

434 limit of 1.75 in core–shell Mie calculations considering the typical size distribution of POA particles

435 (200–800 nm) in the NCP. Furthermore, Alexander et al. (2008) found plenty of primary brown

436 carbon spheres with strong light absorption capacity in East Asian outflow, which indicates that the

437 POA particles could be transported over long distances and still retain their strong light-absorbing

438 properties, and thus can affect the regional and even global radiative forcing. Therefore, we highlight

439 that the "lensing effect", which has been adequately reported on BC particles but not on light-

440 absorbing POA particles in previous studies, should be further considered on these POA particles in

441 radiative forcing models.

442   Considering the adverse effects of residential coal and biomass burning on the haze formation

443 and climate change, we suggest that the governments should continue to implement the "Clean Air

444 Actions" (Zhang and Geng, 2019), especially encourage the use of clean energy such as electricity

445 and natural gas for heating and cooking in rural areas of North China in winter.

446 **Data availability**

447   All data presented in this paper are available upon request. Please contact the corresponding

448 author (liweijun@zju.edu.cn).

449 **Author Contributions**

450   WL and LL designed the research. LL performed the data analysis and wrote the manuscript and

451 WL revised it. JZ and YZ assisted with the sample collection. YS provided the AMS data at the

452 Beijing site. LL, JZ, YZ, LX, QY, and YW carried out the chemical analysis of $PM_{2.5}$ and TEM

453 analysis of individual particles. ZS, YS, DL, and PF contributed to the improvement of this

454 manuscript. All the authors approved the final version of this paper.

455 **Competing interests**

456   The authors declare that they have no conflict of interests.

457 **Acknowledgements**

References

467   Adachi, K., Sedlacek, A. J., Kleinman, L., Chand, D., Hubbe, J. M., and Buseck, P. R.: Volume
468   changes upon heating of aerosol particles from biomass burning using transmission electron
469   microscopy, Aerosol Sci. Tech., 52, 46-56, 10.1080/02786826.2017.1373181, 2018.

470   Adachi, K., Sedlacek, A. J., Kleinman, L., Springston, S. R., Wang, J., Chand, D., Hubbe, J. M.,
471   Shilling, J. E., Onasch, T. B., Kinase, T., Sakata, K., Takahashi, Y., and Buseck, P. R.: Spherical
472   tarball particles form through rapid chemical and physical changes of organic matter in biomass-
473   burning smoke, Proc. Natl. Acad. Sci. U.S.A., 116, 19336-19341, 10.1073/pnas.1900129116,
474   2019.

475   Aden, A. L., and Kerker, M.: Scattering of Electromagnetic Waves from Two Concentric Spheres, J.
476   Appl. Phys., 22, 1242-1246, 10.1063/1.1699834, 1951.

477   Alexander, D. T. L., Crozier, P. A., and Anderson, J. R.: Brown carbon spheres in East Asian outflow
478   and their optical properties, Science, 321, 833-836, 10.1126/science.1155296, 2008.

479   Bohren, C. F., and Huffman, D. R.: Absorption and scattering of light by small particles, John Wiley
480   & Sons, New York, 1983.

481   Bond, T. C., Habib, G., and Bergstrom, R. W.: Limitations in the enhancement of visible light
482   absorption due to mixing state, J. Geophys. Res.-Atmos., 111, D20211, 10.1029/2006jd007315,
483   2006.

484   Bond, T. C., Doherty, S. J., Fahey, D., Forster, P., Berntsen, T., DeAngelo, B., Flanner, M., Ghan, S.,
485   Kärcher, B., and Koch, D.: Bounding the role of black carbon in the climate system: A scientific
486   assessment, J. Geophys. Res.-Atmos., 118, 5380-5552, 10.1002/jgrd.50171, 2013.

487   Chakrabarty, R. K., and Heinson, W. R.: Scaling Laws for Light Absorption Enhancement Due to
488   Nonrefractory Coating of Atmospheric Black Carbon Aerosol, Phys. Rev. Lett., 121, 218701,

489   10.1103/PhysRevLett.121.218701, 2018.

490   Chang, X., Wang, S., Zhao, B., Cai, S., and Hao, J.: Assessment of inter-city transport of particulate

491   matter in the Beijing–Tianjin–Hebei region, Atmos. Chem. Phys., 18, 4843-4858, 10.5194/acp-

492   18-4843-2018, 2018.

493   Chen, S., Xu, L., Zhang, Y., Chen, B., Wang, X., Zhang, X., Zheng, M., Chen, J., Wang, W., Sun, Y.,

494   Fu, P., Wang, Z., and Li, W.: Direct observations of organic aerosols in common wintertime hazes

495   in North China: insights into direct emissions from Chinese residential stoves, Atmos. Chem.

496   Phys., 17, 1259-1270, 10.5194/acp-17-1259-2017, 2017.

497   Chen, X., Wang, H., Lu, K., Li, C., Zhai, T., Tan, Z., Ma, X., Yang, X., Liu, Y., Chen, S., Dong, H.,

498   Li, X., Wu, Z., Hu, M., Zeng, L., and Zhang, Y.: Field Determination of Nitrate Formation

499   Pathway in Winter Beijing, Environ. Sci. Technol., 54, 9243-9253, 10.1021/acs.est.0c00972, 2020.

500   Cheng, Y., Zheng, G., Wei, C., Mu, Q., Zheng, B., Wang, Z., Gao, M., Zhang, Q., He, K., Carmichael,

501   G., Pöschl, U., and Su, H.: Reactive nitrogen chemistry in aerosol water as a source of sulfate

502   during haze events in China, Sci. Adv., 2, e1601530, 10.1126/sciadv.1601530, 2016.

503   Chylek, P., Lee, J. E., Romonosky, D. E., Gallo, F., Lou, S., Shrivastava, M., Carrico, C. M., Aiken,

504   A. C., and Dubey, M. K.: Mie Scattering Captures Observed Optical Properties of Ambient

505   Biomass Burning Plumes Assuming Uniform Black, Brown, and Organic Carbon Mixtures, J.

506   Geophys. Res.-Atmos., 124, 11406-11427, 10.1029/2019jd031224, 2019.

507   Denjean, C., Formenti, P., Picquet-Varrault, B., Katrib, Y., Pangui, E., Zapf, P., and Doussin, J. F.: A

508   new experimental approach to study the hygroscopic and optical properties of aerosols:

509   application to ammonium sulfate particles, Atmos. Meas. Tech., 7, 183-197, 10.5194/amt-7-183-

510   2014, 2014.

511   Du, H., Li, J., Chen, X., Wang, Z., Sun, Y., Fu, P., Li, J., Gao, J., and Wei, Y.: Modeling of aerosol

512   property evolution during winter haze episodes over a megacity cluster in northern China: roles

513   of regional transport and heterogeneous reactions of SO_2, Atmos. Chem. Phys., 19, 9351-9370,

514   10.5194/acp-19-9351-2019, 2019.

515   Ebert, M., Weigel, R., Kandler, K., Günther, G., Molleker, S., Grooß, J. U., Vogel, B., Weinbruch, S.,

516   and Borrmann, S.: Chemical analysis of refractory stratospheric aerosol particles collected within

517   the arctic vortex and inside polar stratospheric clouds, Atmos. Chem. Phys., 16, 8405-8421,

518   10.5194/acp-16-8405-2016, 2016.

519   Fan, X., Liu, J., Zhang, F., Chen, L., Collins, D., Xu, W., Jin, X., Ren, J., Wang, Y., Wu, H., Li, S.,

520   Sun, Y., and Li, Z.: Contrasting size-resolved hygroscopicity of fine particles derived by HTDMA

521   and HR-ToF-AMS measurements between summer and winter in Beijing: the impacts of aerosol

522   aging and local emissions, Atmos. Chem. Phys., 20, 915-929, 10.5194/acp-20-915-2020, 2020.

Feng, Y., Ramanathan, V., and Kotamarthi, V. R.: Brown carbon: a significant atmospheric absorber of solar radiation?, Atmos. Chem. Phys., 13, 8607-8621, 10.5194/acp-13-8607-2013, 2013.

Hoffer, A., Toth, A., Nyiro-Kosa, I., Posfai, M., and Gelencser, A.: Light absorption properties of laboratory-generated tar ball particles, Atmos. Chem. Phys., 16, 239-246, 10.5194/acp-16-239-2016, 2016.

IPCC: Climate change 2013: The Physical Science Basis. Contribution of Working Group I to the Fifth Assessment Report of the Intergovernmental Panel on Climate Change, Cambridge University Press, Cambridge/New York, 2013.

Li, C., He, Q., Schade, J., Passig, J., Zimmermann, R., Meidan, D., Laskin, A., and Rudich, Y.: Dynamic changes in optical and chemical properties of tar ball aerosols by atmospheric photochemical aging, Atmos. Chem. Phys., 19, 139-163, 10.5194/acp-19-139-2019, 2019.

Li, H., Zhang, Q., Zhang, Q., Chen, C., Wang, L., Wei, Z., Zhou, S., Parworth, C., Zheng, B., Canonaco, F., Prevot, A. S. H., Chen, P., Zhang, H., Wallington, T. J., and He, K.: Wintertime aerosol chemistry and haze evolution in an extremely polluted city of the North China Plain: significant contribution from coal and biomass combustion, Atmos. Chem. Phys., 17, 4751-4768, 10.5194/acp-17-4751-2017, 2017.

Li, J., Han, Z., Li, J., Liu, R., Wu, Y., Liang, L., and Zhang, R.: The formation and evolution of secondary organic aerosol during haze events in Beijing in wintertime, Sci. Total Environ., 703, 134937, 10.1016/j.scitotenv.2019.134937, 2020.

Li, M., Fan, X., Zhu, M., Zou, C., Song, J., Wei, S., Jia, W., and Peng, P. a.: Abundance and Light Absorption Properties of Brown Carbon Emitted from Residential Coal Combustion in China, Environ. Sci. Technol., 53, 595-603, 10.1021/acs.est.8b05630, 2019.

Li, W., Zhou, S., Wang, X., Xu, Z., Yuan, C., Yu, Y., Zhang, Q., and Wang, W.: Integrated evaluation of aerosols from regional brown hazes over northern China in winter: Concentrations, sources, transformation, and mixing states, J. Geophys. Res.-Atmos., 116, D09301, 10.1029/2010JD015099, 2011.

Li, W., Shao, L., Zhang, D., Ro, C.-U., Hu, M., Bi, X., Geng, H., Matsuki, A., Niu, H., and Chen, J.: A review of single aerosol particle studies in the atmosphere of East Asia: morphology, mixing state, source, and heterogeneous reactions, J. Clean Prod., 112, 1330-1349, 10.1016/j.jclepro.2015.04.050, 2016a.

Li, W., Sun, J., Xu, L., Shi, Z., Riemer, N., Sun, Y., Fu, P., Zhang, J., Lin, Y., and Wang, X.: A conceptual framework for mixing structures in individual aerosol particles, J. Geophys. Res.-Atmos., 121, 13784-13798, 10.1002/2016JD025252, 2016b.

Li, X., Yang, Y., Liu, S., Zhao, Q., Wang, G., and Wang, Y.: Light absorption properties of brown

557   carbon (BrC) in autumn and winter in Beijing: Composition, formation and contribution of

558   nitrated aromatic compounds, Atmos. Environ., 223, 117289, 10.1016/j.atmosenv.2020.117289,

559   2020.

560   Lin, P., Aiona, P. K., Li, Y., Shiraiwa, M., Laskin, J., Nizkorodov, S. A., and Laskin, A.: Molecular

561   Characterization of Brown Carbon in Biomass Burning Aerosol Particles, Environ. Sci. Technol.,

562   50, 11815-11824, 10.1021/acs.est.6b03024, 2016.

563   Liu, D., Whitehead, J., Alfarra, M. R., Reyes-Villegas, E., Spracklen, D. V., Reddington, C. L., Kong,

564   S., Williams, P. I., Ting, Y.-C., Haslett, S., Taylor, J. W., Flynn, M. J., Morgan, W. T., McFiggans,

565   G., Coe, H., and Allan, J. D.: Black-carbon absorption enhancement in the atmosphere determined

566   by particle mixing state, Nat. Geosci., 10, 184-188, 10.1038/ngeo2901, 2017.

567   Liu, J., Mauzerall, D. L., Chen, Q., Zhang, Q., Song, Y., Peng, W., Klimont, Z., Qiu, X., Zhang, S.,

568   Hu, M., Lin, W., Smith, K. R., and Zhu, T.: Air pollutant emissions from Chinese households: A

569   major and underappreciated ambient pollution source, Proc. Natl. Acad. Sci. U.S.A., 113, 7756-

570   7761, 10.1073/pnas.1604537113, 2016.

571   Liu, L., Kong, S., Zhang, Y., Wang, Y., Xu, L., Yan, Q., Lingaswamy, A. P., Shi, Z., Lv, S., Niu, H.,

572   Shao, L., Hu, M., Zhang, D., Chen, J., Zhang, X., and Li, W.: Morphology, composition, and

573   mixing state of primary particles from combustion sources — crop residue, wood, and solid waste,

574   Sci. Rep., 7, 5047, 10.1038/s41598-017-05357-2, 2017.

575   Liu, L., Zhang, J., Xu, L., Yuan, Q., Huang, D., Chen, J., Shi, Z., Sun, Y., Fu, P., Wang, Z. F., Zhang,

576   D., and Li, W.: Cloud scavenging of anthropogenic refractory particles at a mountain site in North

577   China, Atmos. Chem. Phys., 18, 14681-14693, 10.5194/acp-18-14681-2018, 2018.

578   Liu, P., Zhang, C., Xue, C., Mu, Y., Liu, J., Zhang, Y., Tian, D., Ye, C., Zhang, H., and Guan, J.: The

579   contribution of residential coal combustion to atmospheric $PM_{2.5}$ in northern China during winter,

580   Atmos. Chem. Phys., 17, 11503-11520, 10.5194/acp-17-11503-2017, 2017.

581   Liu, P., Ye, C., Xue, C., Zhang, C., Mu, Y., and Sun, X.: Formation mechanisms of atmospheric nitrate

582   and sulfate during the winter haze pollution periods in Beijing: gas-phase, heterogeneous and

583   aqueous-phase chemistry, Atmos. Chem. Phys., 20, 4153-4165, 10.5194/acp-20-4153-2020, 2020.

584   Ma, Q., Wu, Y., Zhang, D., Wang, X., Xia, Y., Liu, X., Tian, P., Han, Z., Xia, X., Wang, Y., and Zhang,

585   R.: Roles of regional transport and heterogeneous reactions in the $PM_{2.5}$ increase during winter

586   haze episodes in Beijing, Sci. Total Environ., 599, 246-253, 10.1016/j.scitotenv.2017.04.193,

587   2017.

588   Pósfai, M., Simonics, R., Li, J., Hobbs, P. V., and Buseck, P. R.: Individual aerosol particles from

589   biomass burning in southern Africa: 1. Compositions and size distributions of carbonaceous

590   particles, J. Geophys. Res.-Atmos., 108, 8483, 10.1029/2002JD002291, 2003.

591   Reid, J. P., Bertram, A. K., Topping, D. O., Laskin, A., Martin, S. T., Petters, M. D., Pope, F. D., and

592   Rovelli, G.: The viscosity of atmospherically relevant organic particles, Nat. Commun., 9, 956,

593   10.1038/s41467-018-03027-z, 2018.

594   Riemer, N., Ault, A. P., West, M., Craig, R. L., and Curtis, J. H.: Aerosol Mixing State: Measurements,

595   Modeling, and Impacts, Rev. Geophys., 57, 187-249, 10.1029/2018rg000615, 2019.

596   Seinfeld, J. H., and Pandis, S. N.: Atmospheric chemistry and physics: from air pollution to climate

597   change, John Wiley & Sons, 2006.

598   Shi, Z., Vu, T., Kotthaus, S., Harrison, R. M., Grimmond, S., Yue, S., Zhu, T., Lee, J., Han, Y.,

599   Demuzere, M., Dunmore, R. E., Ren, L., Liu, D., Wang, Y., Wild, O., Allan, J., Acton, W. J.,

600   Barlow, J., Barratt, B., Beddows, D., Bloss, W. J., Calzolai, G., Carruthers, D., Carslaw, D. C.,

601   Chan, Q., Chatzidiakou, L., Chen, Y., Crilley, L., Coe, H., Dai, T., Doherty, R., Duan, F., Fu, P.,

602   Ge, B., Ge, M., Guan, D., Hamilton, J. F., He, K., Heal, M., Heard, D., Hewitt, C. N., Hollaway,

603   M., Hu, M., Ji, D., Jiang, X., Jones, R., Kalberer, M., Kelly, F. J., Kramer, L., Langford, B., Lin,

604   C., Lewis, A. C., Li, J., Li, W., Liu, H., Liu, J., Loh, M., Lu, K., Lucarelli, F., Mann, G., McFiggans,

605   G., Miller, M. R., Mills, G., Monk, P., Nemitz, E., O'Connor, F., Ouyang, B., Palmer, P. I., Percival,

606   C., Popoola, O., Reeves, C., Rickard, A. R., Shao, L., Shi, G., Spracklen, D., Stevenson, D., Sun,

607   Y., Sun, Z., Tao, S., Tong, S., Wang, Q., Wang, W., Wang, X., Wang, X., Wang, Z., Wei, L.,

608   Whalley, L., Wu, X., Wu, Z., Xie, P., Yang, F., Zhang, Q., Zhang, Y., Zhang, Y., and Zheng, M.:

609   Introduction to the special issue "In-depth study of air pollution sources and processes within

610   Beijing and its surrounding region (APHH-Beijing)", Atmos. Chem. Phys., 19, 7519-7546,

611   10.5194/acp-19-7519-2019, 2019.

612   Song, J., Li, M., Jiang, B., Wei, S., Fan, X., and Peng, P. a.: Molecular Characterization of Water-

613   Soluble Humic like Substances in Smoke Particles Emitted from Combustion of Biomass

614   Materials and Coal Using Ultrahigh-Resolution Electrospray Ionization Fourier Transform Ion

615   Cyclotron Resonance Mass Spectrometry, Environ. Sci. Technol., 52, 2575-2585,

616   10.1021/acs.est.7b06126, 2018.

617   Stein, A. F., Draxler, R. R., Rolph, G. D., Stunder, B. J. B., Cohen, M. D., and Ngan, F.: NOAA's

618   HYSPLIT Atmospheric Transport and Dispersion Modeling System, Bull. Amer. Meteorol. Soc.,

619   96, 2059-2077, 10.1175/bams-d-14-00110.1, 2016.

620   Sun, J., Zhi, G., Hitzenberger, R., Chen, Y., Tian, C., Zhang, Y., Feng, Y., Cheng, M., Zhang, Y., Cai,

621   J., Chen, F., Qiu, Y., Jiang, Z., Li, J., Zhang, G., and Mo, Y.: Emission factors and light absorption

622   properties of brown carbon from household coal combustion in China, Atmos. Chem. Phys., 17,

623   4769-4780, 10.5194/acp-17-4769-2017, 2017.

624   Sun, Y., Jiang, Q., Wang, Z., Fu, P., Li, J., Yang, T., and Yin, Y.: Investigation of the sources and

625   evolution processes of severe haze pollution in Beijing in January 2013, J. Geophys. Res.-Atmos.,

626   119, 4380-4398, 10.1002/2014jd021641, 2014.

627 Sun, Y., Chen, C., Zhang, Y., Xu, W., Zhou, L., Cheng, X., Zheng, H., Ji, D., Li, J., Tang, X., Fu, P.,

628   and Wang, Z.: Rapid formation and evolution of an extreme haze episode in Northern China

629   during winter 2015, Sci. Rep., 6, 27151, 10.1038/srep27151, 2016.

630 Toon, O. B., and Ackerman, T. P.: Algorithms for the calculation of scattering by stratified spheres,

631   Appl. Opt., 20, 3657-3660, 10.1364/ao.20.003657, 1981.

632 Wang, B., Harder, T. H., Kelly, S. T., Piens, D. S., China, S., Kovarik, L., Keiluweit, M., Arey, B. W.,

633   Gilles, M. K., and Laskin, A.: Airborne soil organic particles generated by precipitation, Nat.

634   Geosci., 9, 433-437, 10.1038/NGEO2705, 2016.

635 Wang, J., Nie, W., Cheng, Y., Shen, Y., Chi, X., Wang, J., Huang, X., Xie, Y., Sun, P., Xu, Z., Qi, X.,

636   Su, H., and Ding, A.: Light absorption of brown carbon in eastern China based on 3-year multi-

637   wavelength aerosol optical property observations and an improved absorption Ångström exponent

638   segregation method, Atmos. Chem. Phys., 18, 9061-9074, 10.5194/acp-18-9061-2018, 2018.

639 Wang, J., Li, J., Ye, J., Zhao, J., Wu, Y., Hu, J., Liu, D., Nie, D., Shen, F., Huang, X., Huang, D. D.,

640   Ji, D., Sun, X., Xu, W., Guo, J., Song, S., Qin, Y., Liu, P., Turner, J. R., Lee, H. C., Hwang, S.,

641   Liao, H., Martin, S. T., Zhang, Q., Chen, M., Sun, Y., Ge, X., and Jacob, D. J.: Fast sulfate

642   formation from oxidation of SO_2 by NO_2 and HONO observed in Beijing haze, Nat. Commun.,

643   11, 2844, 10.1038/s41467-020-16683-x, 2020.

644 Wang, X., Heald, C. L., Ridley, D. A., Schwarz, J. P., Spackman, J. R., Perring, A. E., Coe, H., Liu,

645   D., and Clarke, A. D.: Exploiting simultaneous observational constraints on mass and absorption

646   to estimate the global direct radiative forcing of black carbon and brown carbon, Atmos. Chem.

647   Phys., 14, 10989-11010, 10.5194/acp-14-10989-2014, 2014.

648 Wang, Y., Liu, F., He, C., Bi, L., Cheng, T., Wang, Z., Zhang, H., Zhang, X., Shi, Z., and Li, W.:

649   Fractal Dimensions and Mixing Structures of Soot Particles during Atmospheric Processing,

650   Environ. Sci. Technol. Lett., 4, 487-493, 10.1021/acs.estlett.7b00418, 2017.

651 West, J. J., Cohen, A., Dentener, F., Brunekreef, B., Zhu, T., Armstrong, B., Bell, M. L., Brauer, M.,

652   Carmichael, G., and Costa, D. L.: What We Breathe Impacts Our Health: Improving

653   Understanding of the Link between Air Pollution and Health, Environ. Sci. Technol., 50, 4895-

654   4904, 10.1021/acs.est.5b03827, 2016.

655 Wu, C., Wu, D., and Yu, J. Z.: Quantifying black carbon light absorption enhancement with a novel

656   statistical approach, Atmos. Chem. Phys., 18, 289-309, 10.5194/acp-18-289-2018, 2018.

657 Xie, C., Xu, W., Wang, J., Wang, Q., Liu, D., Tang, G., Chen, P., Du, W., Zhao, J., Zhang, Y., Zhou,

658   W., Han, T., Bian, Q., Li, J., Fu, P., Wang, Z., Ge, X., Allan, J., Coe, H., and Sun, Y.: Vertical

659   characterization of aerosol optical properties and brown carbon in winter in urban Beijing, China,

660   Atmos. Chem. Phys., 19, 165-179, 10.5194/acp-19-165-2019, 2019.

661 Xing, L., Fu, T. M., Cao, J. J., Lee, S. C., Wang, G. H., Ho, K. F., Cheng, M. C., You, C. F., and Wang,

662   T. J.: Seasonal and spatial variability of the OM/OC mass ratios and high regional correlation

663   between oxalic acid and zinc in Chinese urban organic aerosols, Atmos. Chem. Phys., 13, 4307-

664   4318, 10.5194/acp-13-4307-2013, 2013.

665 Xu, J., Srivastava, D., Wu, X., Hou, S., Vu, T. V., Liu, D., Sun, Y., Vlachou, A., Moschos, V., Salazar,

666   G., Szidat, S., Prevot, A., Fu, P., Harrison, R. M., and Shi, Z.: An evaluation of source

667   apportionment of fine OC and $PM_{2.5}$ by multiple methods: APHH-Beijing campaigns as a case

668   study, Faraday Discussions, 10.1039/D0FD00095G, 2020.

669 Xu, W., Sun, Y., Wang, Q., Zhao, J., Wang, J., Ge, X., Xie, C., Zhou, W., Du, W., Li, J., Fu, P., Wang,

670   Z., Worsnop, D. R., and Coe, H.: Changes in Aerosol Chemistry From 2014 to 2016 in Winter in

671   Beijing: Insights From High-Resolution Aerosol Mass Spectrometry, J. Geophys. Res.-Atmos.,

672   124, 1132-1147, 10.1029/2018jd029245, 2019.

673 Yan, C., Zheng, M., Bosch, C., Andersson, A., Desyaterik, Y., Sullivan, A. P., Collett, J. L., Zhao, B.,

674   Wang, S., He, K., and Gustafsson, Ö.: Important fossil source contribution to brown carbon in

675   Beijing during winter, Sci. Rep., 7, 43182, 10.1038/srep43182, 2017.

676 Yu, H., Li, W., Zhang, Y., Tunved, P., Dall'Osto, M., Shen, X., Sun, J., Zhang, X., Zhang, J., and Shi,

677   Z.: Organic coating on sulfate and soot particles during late summer in the Svalbard Archipelago,

678   Atmos. Chem. Phys., 19, 10433-10446, 10.5194/acp-19-10433-2019, 2019.

679 Zhang, J., Liu, L., Wang, Y., Ren, Y., Wang, X., Shi, Z., Zhang, D., Che, H., Zhao, H., Liu, Y., Niu,

680   H., Chen, J., Zhang, X., Lingaswamy, A. P., Wang, Z., and Li, W.: Chemical composition, source,

681   and process of urban aerosols during winter haze formation in Northeast China, Environ. Pollut.,

682   231, 357-366, 10.1016/j.envpol.2017.07.102, 2017.

683 Zhang, J., Liu, L., Xu, L., Lin, Q., Zhao, H., Wang, Z., Guo, S., Hu, M., Liu, D., Shi, Z., Huang, D.,

684   and Li, W.: Exploring wintertime regional haze in northeast China: role of coal and biomass

685   burning, Atmos. Chem. Phys., 20, 5355-5372, 10.5194/acp-20-5355-2020, 2020.

686 Zhang, Q., and Geng, G.: Impact of clean air action on $PM_{2.5}$ pollution in China, Sci. China-Earth

687   Sci., 62, 1845-1846, 10.1007/s11430-019-9531-4, 2019.

688 Zhang, Y., Yuan, Q., Huang, D., Kong, S., Zhang, J., Wang, X., Lu, C., Shi, Z., Zhang, X., Sun, Y.,

689   Wang, Z., Shao, L., Zhu, J., and Li, W.: Direct observations of fine primary particles from

690   residential coal burning: insights into their morphology, composition, and hygroscopicity, J.

691   Geophys. Res.-Atmos., 123, 12964-12979, 10.1029/2018JD028988, 2018.

692 Zheng, G. J., Duan, F. K., Su, H., Ma, Y. L., Cheng, Y., Zheng, B., Zhang, Q., Huang, T., Kimoto, T.,

693   Chang, D., Pöschl, U., Cheng, Y. F., and He, K. B.: Exploring the severe winter haze in Beijing:

694   the impact of synoptic weather, regional transport and heterogeneous reactions, Atmos. Chem.

695   Phys., 15, 2969-2983, 10.5194/acp-15-2969-2015, 2015.

696 Zhong, J., Zhang, X., Wang, Y., Wang, J., Shen, X., Zhang, H., Wang, T., Xie, Z., Liu, C., Zhang, H.,

697   Zhao, T., Sun, J., Fan, S., Gao, Z., Li, Y., and Wang, L.: The two-way feedback mechanism

698   between unfavorable meteorological conditions and cumulative aerosol pollution in various haze

699   regions of China, Atmos. Chem. Phys., 19, 3287-3306, 10.5194/acp-19-3287-2019, 2019.

700
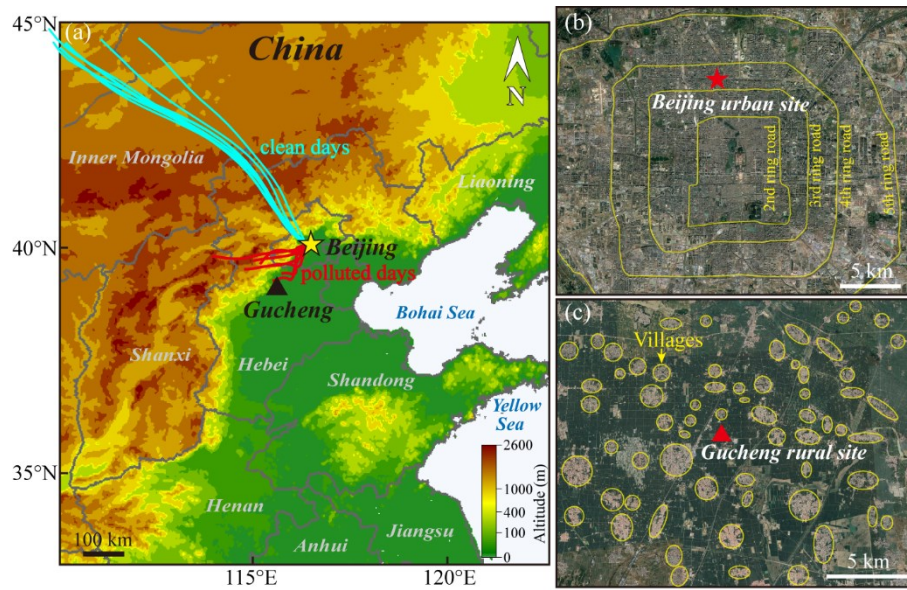
Figures

Figure 1. Locations of Beijing and Gucheng in the North China Plain (a) and the expanded view of surrounding topographies around the Beijing urban site (b) and Gucheng rural site (c). The 24-h backward trajectories of air masses ending at the height of 100 m (a.g.l) over the Beijing urban site in clean days (20–23 November) and polluted days (24–27 November) during the observation are also shown in (a). (Map copyright @2020 Google Maps)
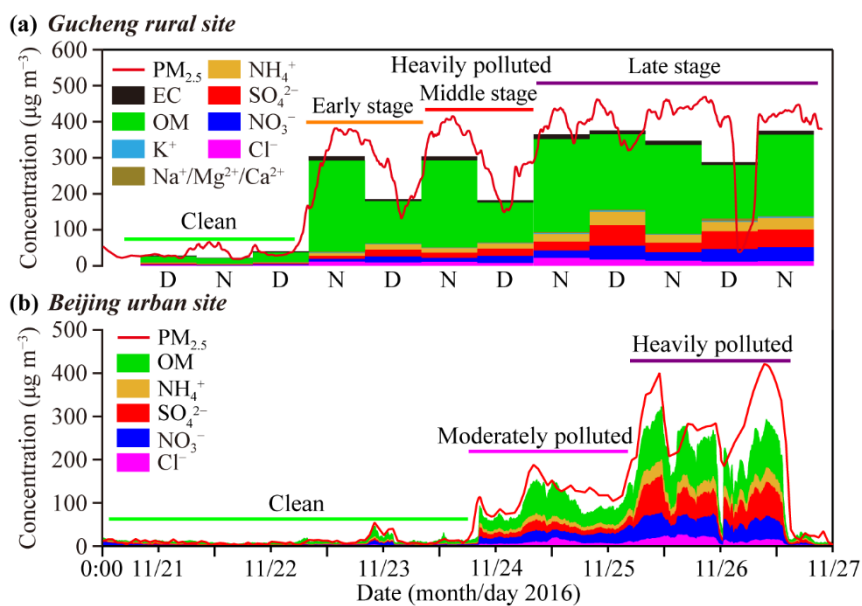
Figure 2. Time series of PM$_{2.5}$ and major aerosol chemical species at the (a) Gucheng rural site and (b) Beijing urban site. Chemical species were obtained by offline analysis of daytime (D) and nighttime (N) PM$_{2.5}$ filter samples at the rural site and were obtained by online analysis of NR-PM$_1$ using a high-resolution aerosol mass spectrometer (HR-AMS) at the urban site. The different periods of the haze episode at rural and urban sites are marked in this figure.

713
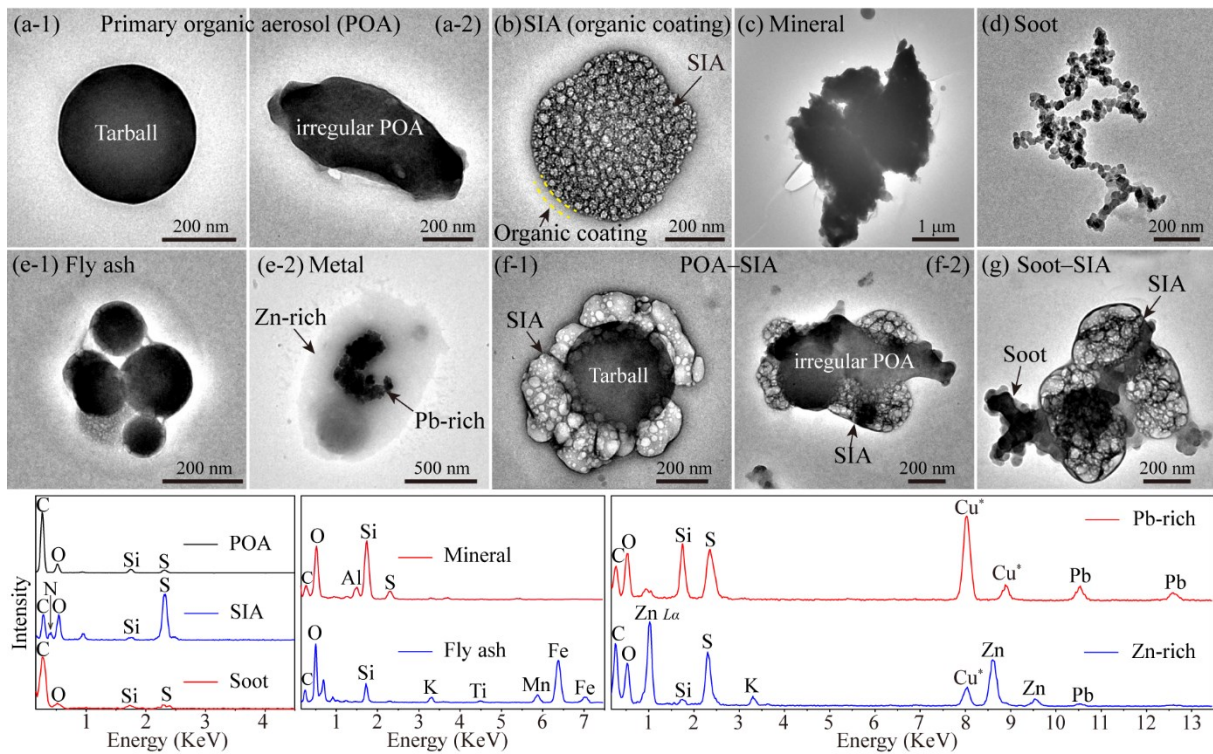
714 Figure 3. Typical transmission electron microscopy (TEM) images and energy-dispersive X-ray spectrometry (EDS)

715 spectra showing the morphology, composition, and mixing structures of different individual particle types. (a)

716 primary organic aerosol (POA) particles with (a-1) spherical (i.e., tarball) or (a-2) irregular shapes; (b) secondary

717 inorganic aerosol (SIA) particle with secondary organic coating; (c) mineral; (d) soot; (e-1) fly ash and (e-2) metal;

718 (f) internally mixed POA particle with SIA coating (POA–SIA); (g) internally mixed soot particle with SIA coating

719 (soot–SIA).

720
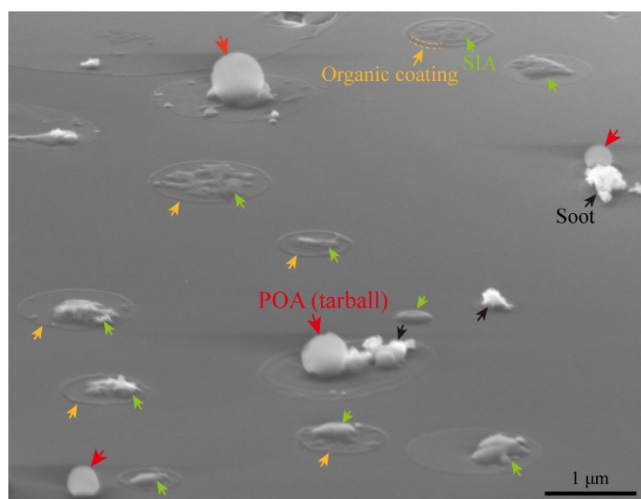
Figure 4. Scanning electron microscopy (SEM) image acquired in the secondary electron (SE2) mode at a 75° tilt angle showing the surface morphology of individual particles in the vertical dimension. The red, black, green, and orange arrows indicate primary organic aerosol (POA) particle (mainly tarball), soot particle, secondary inorganic aerosol (SIA) particle, and secondary organic coating, respectively.
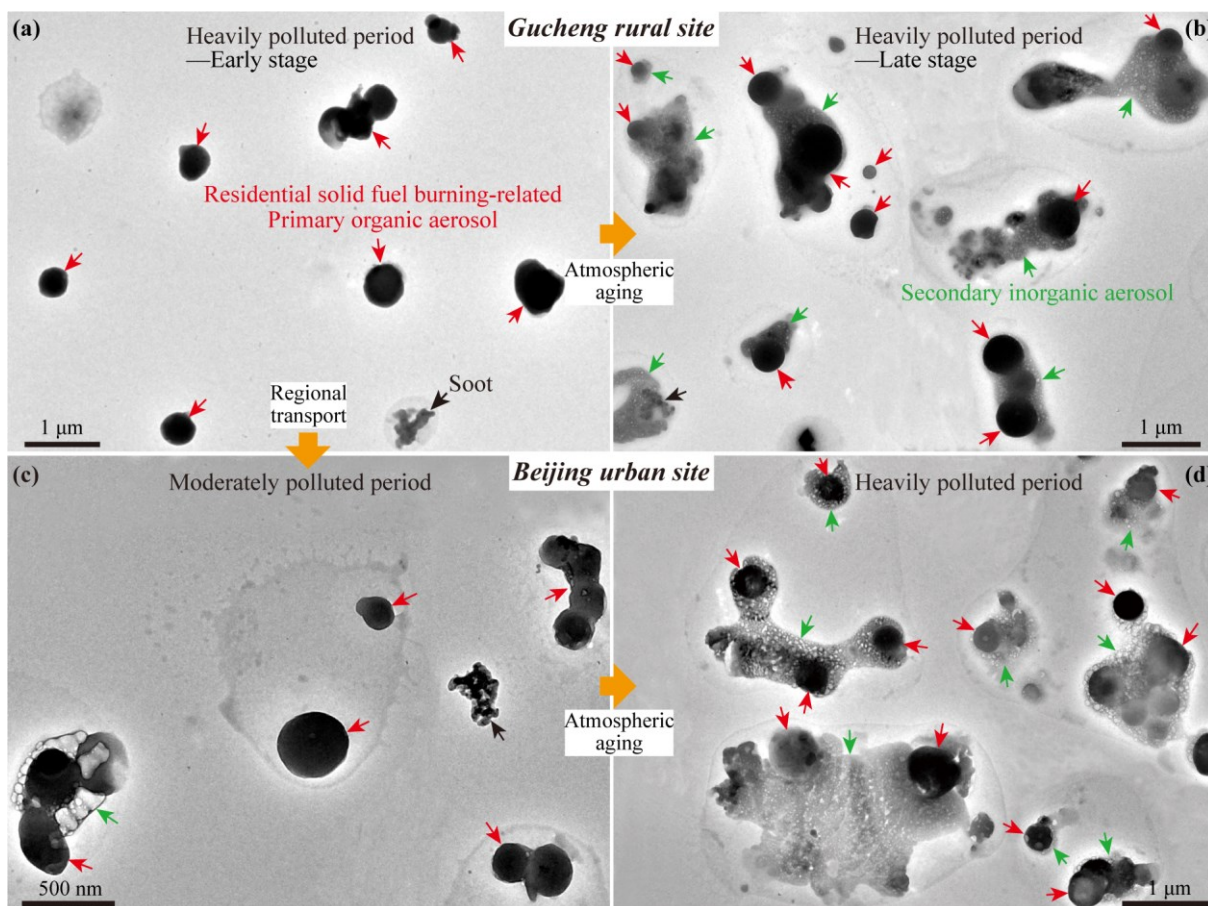
31
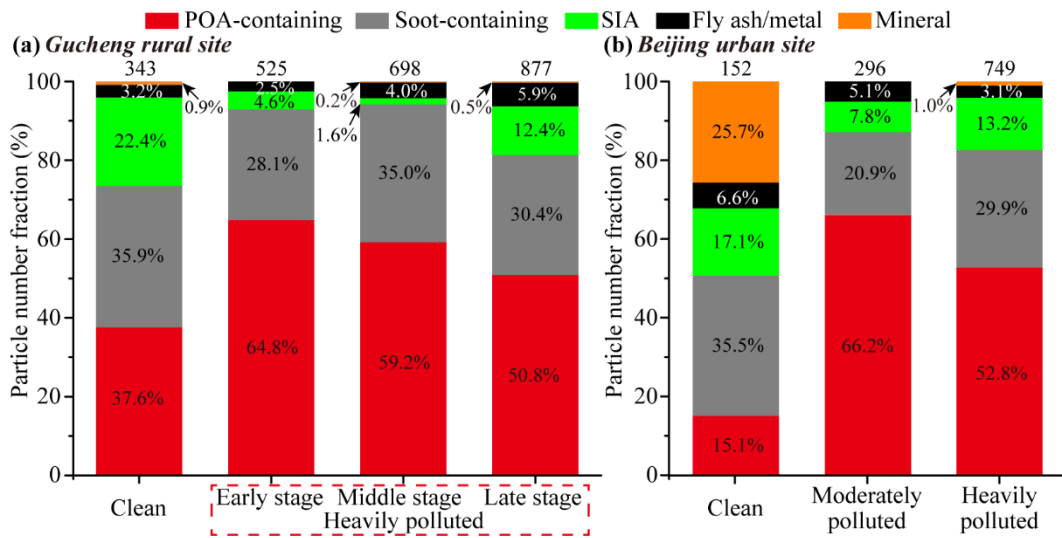
Figure 5. Relative abundance of different particle types in different periods at the (a) Gucheng rural site and (b) Beijing urban site. The numbers of analyzed particles in different periods are shown on the top of each column.

Figure 6. TEM images showing individual particles collected in the (a) early stage and (b) late stage of heavily polluted period at the Gucheng rural site and in the (c) moderately polluted and (d) heavily polluted periods at the Beijing urban site. The red, green, and black arrows indicate primary organic aerosol (POA) particle, secondary inorganic aerosol (SIA) particle, and soot particle, respectively.
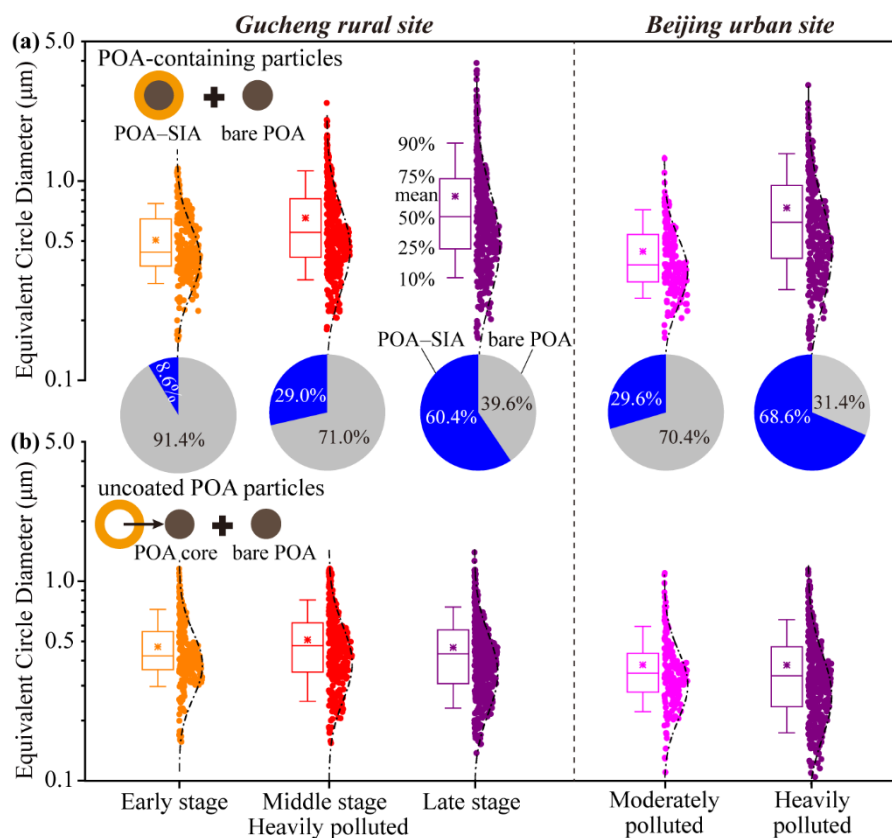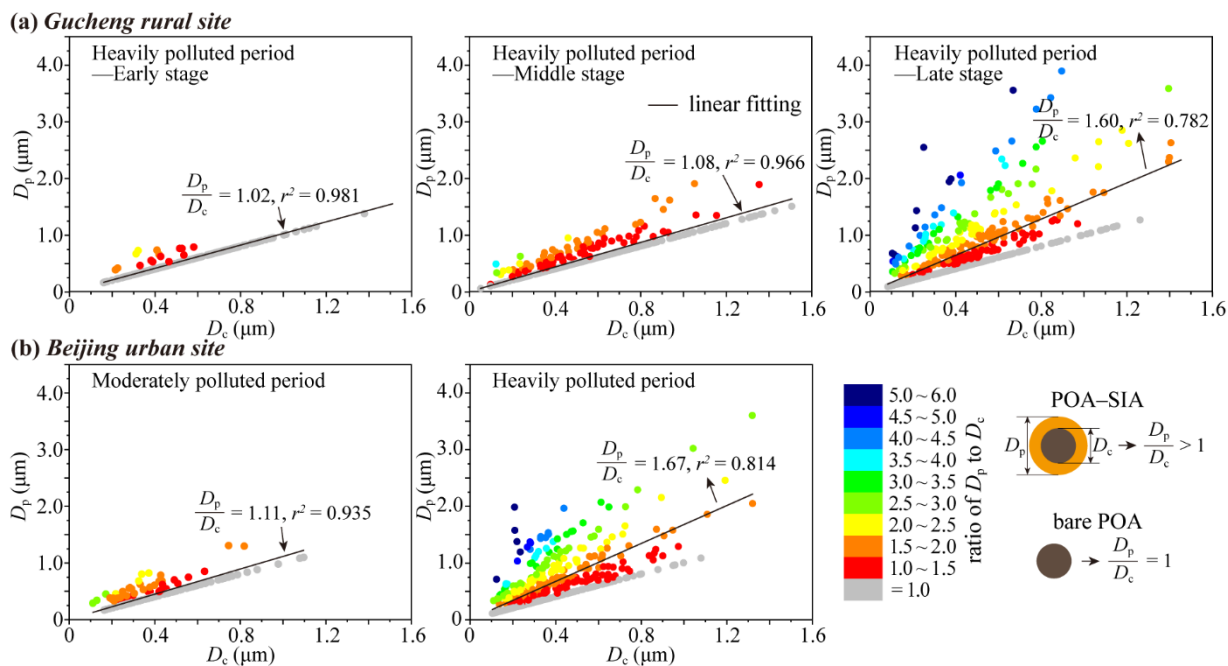
Figure 7. Box plots showing equivalent circle diameters (ECD) of (a) POA-containing particles (including core–shell POA–SIA and bare POA) and (b) uncoated POA particles (including POA cores without SIA shell and bare POA) in different polluted periods at the Gucheng rural site and Beijing urban site. The solid circles (right of the box) represent the ECD of individual particles with lognormal distributions. The pie charts present the relative number fractions between POA–SIA and bare POA in different polluted periods.
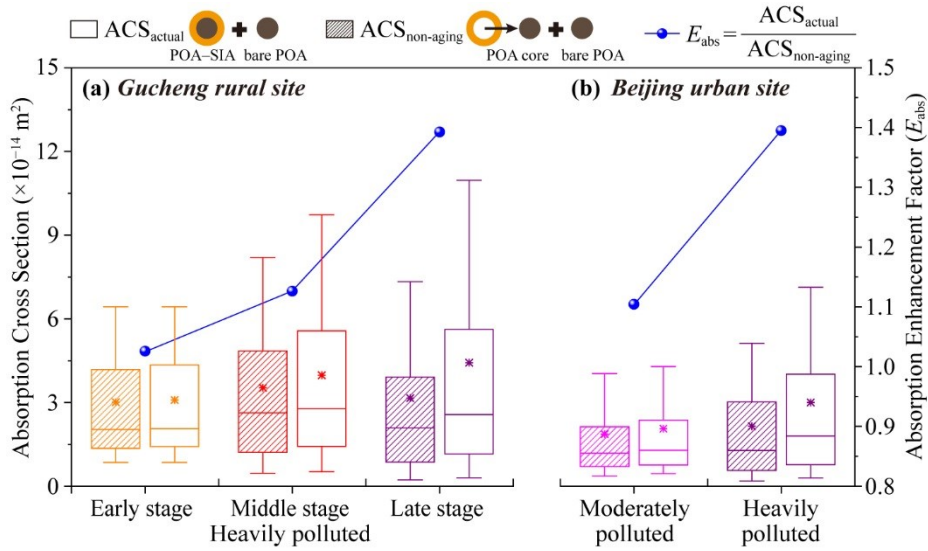
Figure 8. Relationship between the diameter of POA-containing particle (D_p) and its POA core (D_c) in the early stage, middle stage, and late stage of heavily polluted period at the Gucheng rural site (a) and in the moderately polluted and heavily polluted periods at the Beijing urban site (b).

Figure 9. Box plots of light absorption cross sections (ACS) of individual POA-containing particles (including core–shell POA–SIA and bare POA) under the actual scenario (ACS_{actual}) and uncoated POA particles (including POA cores without SIA shell and bare POA) under the particle non-aging scenario ($ACS_{non-aging}$) at the wavelength of 550 nm; and variations in the light absorption enhancement factors (E_{abs}, i.e., ratio of ACS_{actual} to $ACS_{non-aging}$) in different polluted periods at the (a) Gucheng rural site and (b) Beijing urban site. A refractive index of $1.55-0i$ for non-light-absorbing SIA coating (Denjean et al., 2014) and $1.67-0.27i$ for light-absorbing POA core (Alexander et al., 2008) were adopted at the wavelength of 550 nm. The box represents the 25th (lower line), 50th (middle line), and 75th (top line) percentiles; the asterisk in the box represents the mean value; and the end lines of the vertical bars represent the 10th (below the box) and 90th (above the box) percentiles.
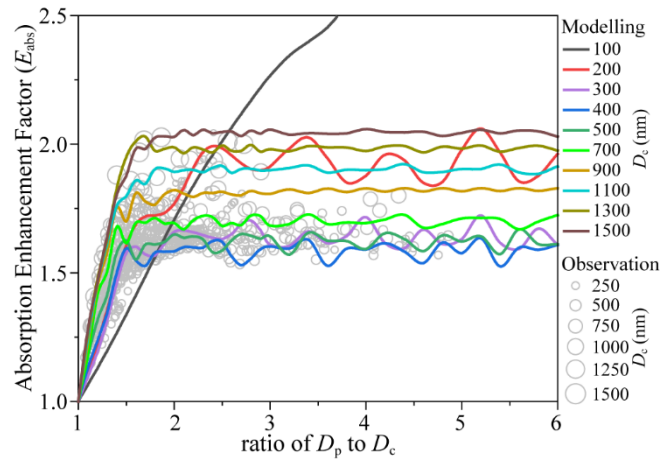
Figure 10. Mie theory-calculated light absorption enhancement factors (E_{abs}) of modelled core–shell POA–SIA particles (i.e., ratio of $ACS_{POA–SIA}$ to $ACS_{POA\ core}$) with different POA core diameters (D_c) as a function of particle-to-core diameter ratio (D_p/D_c) at the wavelength of 550 nm (solid lines). A refractive index of $1.55−0i$ for non-light-absorbing SIA coating (Denjean et al., 2014) and $1.67−0.27i$ for light-absorbing POA core (Alexander et al., 2008) were adopted at the wavelength of 550 nm. The open circles represent all the observed POA–SIA particles during the whole polluted periods at Gucheng rural and Beijing urban sites.